Oxygen Ion Escape from Venus is modulated by Ultra-Low-Frequency Waves

R. Jarvinen[1,2], **M. Alho**[1], **E. Kallio**[1] **and T. I. Pulkkinen**[3,1]

[1]Department of Electronics and Nanoengineering, School of Electrical Engineering, Aalto University, Espoo, Finland
[2]Finnish Meteorological Institute, Helsinki, Finland
[3]Department of Climate and Space Sciences and Engineering, University of Michigan, Ann Arbor, Michigan, USA

Key Points:

- A global hybrid simulation predicts fluctuations in the O^+ escape from Venus.
- The fluctuations are associated with the foreshock ULF waves, which modulate the acceleration of heavy pickup ions.
- Upstream waves need to be taken into account in the interpretation of heavy ion erosion from unmagnetized planets.

This is the author manuscript accepted for publication and has undergone full peer review but has not been through the copyediting, typesetting, pagination and proofreading process, which may lead to differences between this version and the Version of Record. Please cite this article as doi: 10.1029/2020GL087462

Corresponding author: R. Jarvinen, `riku.jarvinen@aalto.fi`

Abstract

We study the solar wind driven, nonthermal escape of O^+ ions from Venus in a global hybrid simulation. In the model, a well-developed ion foreshock forms ahead of the Venusian quasi-parallel bow shock under nominal upstream conditions. Large-scale magnetosonic ultra-low-frequency (ULF) waves at 20–30-second period are excited, and convect downstream along the foreshock with the solar wind. We show that the foreshock ULF waves transmit through the bow shock in the downstream region and interact with the planetary ion acceleration, causing 25% peak-to-peak fluctuations in the O^+ escape rate. These results demonstrate the importance of upstream plasma waves on the energization and escape of heavy ions from the planetary atmospheres.

1 Introduction

Our sister planet Venus is extremely dry as compared to the Earth, and has likely lost a significant amount of water during the history of the solar system (*Greenwood et al.*, 2018). It is still under debate how the water was lost, and how much different atmospheric erosion processes have changed the planet's volatile inventories. Being an unmagnetized body, the upper atmosphere of Venus is subject to the direct, non-collisional solar wind-driven escape of ionized heavy elements, which are gravitationally bound to the atmosphere (*Futaana et al.*, 2017). In the Venus-solar wind interaction, part of the ionized ionospheric and exospheric particle populations are accelerated to the escape velocity and are lost to space. At Earth the solar wind influence on the atmospheric erosion is mediated by the geomagnetic field (*Yau et al.*, 1985; *Nilsson et al.*, 2012). As the present-day heavy element loss rates from Venus are not very significant on the time-scales of planetary evolution, it is essential to quantify all mechanisms for the atmospheric escape to produce a realiable estimate of the volatile erosion history of the planet (*Persson et al.*, 2018). Such results will also be relevant for Mars as well as for any other unmagnetized body in the solar or exoplanetary systems.

The induced magnetosphere of Venus forms when the interplanetary magnetic field (IMF) piles up against the ionosphere creating the magnetic barrier. Similar to other planets, a bow shock forms the boundary between the supermagnetosonic solar wind and the heated and turbulent magnetosheath plasma enveloping the induced magnetospheric boundary or the magnetopause (*Russell et al.*, 1988; *Zhang et al.*, 2008a,b). The foreshock region is magnetically connected to the bow shock, which allows backstreaming of the suprathermal charged particles (*Eastwood et al.*, 2005; *Omidi et al.*, 2017). The interaction between the suprathermal and incident solar wind populations drive a multitude of plasma waves, especially the large-scale ultra-low-frequency (ULF) magnetosonic waves, which are typically found under quasi-parallel conditions where the angle between the shock surface normal and the IMF is smaller than about 45° (*Keiling et al.*, 2016; *Fränz et al.*, 2017). Such waves can have significant effects on the dynamic processes in the planetary space environments especially at unmagnetized bodies, where the bow shock forms close to the planet (*Lundin*, 2011).

Acceleration mechanisms of ions away from unmagnetized planets include several processes or "escape channels", which can be classified according to the ion energy and region around the planet (*Dubinin et al.*, 2011; *Brain et al.*, 2016). Significant cold or low energy ion escape is found especially in the induced magnetotail as well as at low altitudes near the ionosphere. At higher altitudes the largest-scale escape channel is the ion pickup but also several smaller scale channels exist. Relative escape rates through different channels can vary somewhat as a function of the upstream conditions and observed ion energy (*Fedorov et al.*, 2011; *Dong et al.*, 2017).

In the high-energy escape, the pickup ions form the heavy ion plume (*Nordström et al.*, 2013; *Liemohn et al.*, 2014; *Wei et al.*, 2017; *Jarvinen et al.*, 2016). In addition to the so-called "north-south" asymmetry, the plume exhibits a significant hemispheric "dawn-dusk" asymmetry in the direction perpendicular to the plane defined by the undisturbed solar wind velocity and convection electric field vectors, when the upstream IMF has a strong flow-aligned component as is typical at the orbit of Venus (*McComas et al.*, 1986; *Jarvinen et al.*, 2013). Interestingly, the dawn-dusk asymmetry means that the E×B drift turns the escaping heavy ions towards the hemisphere of the quasi-parallel bow shock and the ion foreshock rather than the opposite hemisphere (*Jarvinen et al.*, 2013; *Jarvinen and Kallio*, 2014). The acceleration of planetary ions by convecting magnetic field fluctuations in the Venus' magnetosheath downstream from the quasi-parellel bow shock, like the foreshock ULF waves, has been suggested in test particle studies (*Luhmann et al.*, 1987), and recently discussed based on observations (*Lundin et al.*, 2011; *Collinson et al.*, 2018; *Franco et al.*, 2020).

Different aspects of the solar wind driven ion escape from unmagnetized planets have been studied in self-consistent plasma models including hybrid and magnetohydrodynamic codes (*Ledvina et al.*, 2008). While several studies have focused on the escape rates and the structure of the induced magnetosphere (e.g. *Brain et al.*, 2010, and references therein), the interaction of the ULF waves and the ion escape has not been analyzed in a self-consistent model. Here we report on a new finding that the foreshock ULF waves have significant effects on the Venusian heavy ion acceleration in the induced magnetosphere and escape.

2 Model

We simulate the Venus-solar wind interaction using the hybrid model platform *RHybrid* (*Jarvinen et al.*, 2018, 2020). In the model, ions of solar wind and planetary origin are treated as macroscopic particle clouds (macroparticles) and their motion is determined by the Lorentz force. Electrons are an isothermal, charge-neutralizing and massless fluid. Planetary ions are produced via photoionization of hydrogen and oxygen exosphere coronae and via an upward emission of ionospheric oxygen ions from the model inner boundary. The production rates and profiles of planetary ions are the same as in our earlier Venus works and correspond to solar minimum conditions (*Jarvinen et al.*, 2009, 2013). The solar wind is injected through the front wall, and macroparticles are removed from the simulation as they encounter simulation boundaries.

The simulation run uses nominal, stationary upstream conditions at Venus (*Slavin and Holzer*, 1981) with Parker spiral angle of 36° and the flow-aligned component of the IMF stronger than the perpendicular component. The simulation setup and the algorithm are similar to our earlier studies of the Venus and Mars space environments (*Kallio et al.*, 2010; *Jarvinen et al.*, 2013), with the exception that the number of grid cells and macroparticles are much higher in the current parallel code compared to the sequential code. See Table 1 for details of the simulation run and *Kallio and Janhunen* (2003) for further details of the algorithm.

We use a planet-centered coordinate system, where the x-axis is antiparallel to the incident, undisturbed solar wind flow, the y-axis is aligned along the perpendicular IMF component to the undisturbed solar wind flow, and the z-axis completes the right-handed coordinate system and, thus, is along the convection electric field in the undisturbed solar wind flow. The hemisphere where the upstream solar wind convection electric field points away from the planet ($z > 0$) is termed the $+E_{\mathrm{SW}}$ hemisphere and the $y < 0$ hemisphere is termed the foreshock hemisphere. The radius of Venus ($R_{\mathrm{V}} = 6051.8$ km) is used as the unit of length in the figures and the text.

Temporal properties of the solar wind and planetary plasma and fields were recorded at every time step between $t = 250...450$ s in grid cells centered at the points P1 $(x, y, z) = (0.56, -4.24, 0.01)R_{\mathrm{V}}$, P2 $(x, y, z) = (-2.19, -1.19, 0.01)R_{\mathrm{V}}$, and P3 $(x, y, z) = (0.01, -0.96, 0.86)R_{\mathrm{V}}$. Figure 1 shows the locations of the points in the simulation domain.

3 Results

Figure 1 shows a snapshot of the Venus induced magnetosphere and the O^+ bulk flux (see Movie S01 in the supplementary material for the dynamics of these parameters). The induced magnetosphere is clearly visible in the B_z-component with the bow shock lineating the outermost boundary and the magnetosheath separating the induced magnetotail from the upstream solar wind. The foreshock upstream of the bow shock on the $y < 0$ hemisphere includes large-scale waves visible in B_z. Both parameters in the figure and the movie show ongoing variations at different temporal and spatial scales even though the solar wind driving is stationary.

The O^+ escape rate is analyzed in detail in Figure 2. The O^+ net fluxes (outward flux - inward flux) integrated over spherical shells at different altitudes show the radial evolution of the escape rate dynamics. The lowest altitudes show little fluctuations in the O^+ escape, but the fluctuations intensify with increasing altitude. The escape rate through the outer boundaries of the simulation domain shows fluctuations with about 25% peak-to-peak amplitude, with maximum power spectral density at the frequency of 0.03-0.04 Hz (25-33 s) (Figure S04 in the supplementary material). Spectral maxima at about the same frequency range can be identified at the spherical shells $r \geq 1.5R_{\mathrm{V}}$.

The net escape rate increases to about 94% of the value at the domain outer boundary from the $r = 1.1R_{\mathrm{V}}$ to $1.5R_{\mathrm{V}}$ shell. This low-altitude increase is caused by a drop in the planetward O^+ rate and photoion production between the two shells. The planetward O^+ rate is three orders of magnitude smaller than the net escape rate at the $r = 2.7R_{\mathrm{V}}$ shell. The O^+ escape rates through the outer boundaries are $2.9{\times}10^{24}$ s^{-1} for the ionospheric population and 1.9×10^{24} s^{-1} for the exospheric photoions.

Figure 3 displays the magnetic field time series in the foreshock (P1), in the quasi-parallel equatorial, night-side magnetosheath (P2) and in the low-altitude quasi-parallel terminator region on the $+E_{\mathrm{SW}}$ hemisphere (P3). Periodic large-scale waves are evident at the three points with the maximum power spectral density in the ULF frequency range of about 0.03-0.05 Hz (20-33 s) (Figure S05 in the supplementary material). In this study, we refer to these waves as the 20–30-s waves. At P1, the average B_z is nearly zero as expected due to the upstream conditions, whereas at P2 the average B_z is slightly negative and at P3 positive because of the IMF piling up and draping around Venus.

The electron density and the magnitude of the magnetic field are positively correlated for the foreshock waves. Minimum variance analysis (MVA) shows that the foreshock waves are left-hand polarized and travel at a small angle ($< 10°$) with respect to the magnetic field in the simulation frame. An estimated wave phase speed is below the solar wind bulk velocity projected in the direction of the wave propagation, which implies that the foreshock waves are propagating upstream and are right-hand polarized in the plasma frame (see details of the MVA and phase speed determination in the model in *Jarvinen et al.*, 2020). Taken together, these imply that the foreshock ULF waves are oblique fast magnetosonic modes excited by the backstreaming solar wind ions in the foreshock. This in agreement with *in situ* spacecraft observations by Pioneer Venus Orbiter (*Luhmann et al.*, 1983) and Venus Express (*Shan et al.*, 2016) as well as with previous global hybrid models (*Omidi et al.*, 2017).

The O^+ energization is analyzed in Figure 4. The parameter $q\vec{E}{\cdot}\vec{U}(O^+)$ gives the average net work by the electric field on an O^+ ion in each grid cell per unit time. In the foreshock region (P1), the power varies from negative to positive implying temporal changes from bulk deceleration to acceleration. This is due to a low O^+ density and statistical variations of the velocity of exospheric photoions sometimes aligned and sometimes anti-aligned with the electric field in the upstream region. In the nightside magnetosheath at P2, the O^+ flux is also dominated by the exospheric population, but the density is higher and, thus, the escaping O^+ flow is more organized along the tail and the electric field than at P1. The O^+ density is highest at the quasi-parallel terminator (P3), and dominated by the ionospheric population. The average power is positive, indicating net acceleration at both downstream locations. The points P1-P3 show modulation of $q\vec{E}{\cdot}\vec{U}(O^+)$ with the maximum power spectral density in the ULF frequency range of about 0.02-0.05 Hz (20-50 s) (Figure S06 in the supplementary material).

4 Discussion

Using a global hybrid simulation, we show that the upstream ULF waves interact with the O^+ ion acceleration and escape from Venus. In the model, under nominal, stationary solar wind conditions, large-scale 20–30-s magnetosonic foreshock ULF waves are excited in the ion foreshock and they convect downstream with the solar wind flow and transmit through the quasi-parallel bow shock (*Shan et al.*, 2014; *Dubinin and Fraenz*, 2016). The waves interact with the O^+ energization in the upstream, near-equatorial magnetosheath and low-altitude terminator regions on the foreshock hemisphere (Figure 4).

The coupling between the O^+ acceleration and the ULF waves at the frequency range of the foreshock ULF waves is evident in the upstream region (x = -1.5 ... 0.5 R_V, y = -3.0 ... -2.0 R_V), and in the quasi-parallel magnetosheath (x = -3.0 ... -1.5 R_V, y = -2.0 ... -1.0 R_V) (Figure 1, Movie S02 in the supplementary material). Furthermore, the coupling of the O^+ energization and B_z is present already at the low-altitude region on the spherical shell at $r = 1.29 R_\mathrm{V}$ where the vantage point P3 is located (Figures 2-4, Movie S03 in the supplementary material). The ULF waves and the O^+ modulation at the frequency range of the foreshock ULF waves are clearly visible on the quasi-parallel side of the shell (longitude = 240 ... 360° and latitude = -10 ... 60°) from t = 100 s onwards.

The dynamics of the escaping O^+ ions in the model can be shown to be consistent with theoretical consideration of an idealized pickup process (*Jarvinen and Kallio*, 2014): A scatter-free motion of a pickup ion starting at rest in homogeneous electric and magnetic fields includes periods with the z-component of the velocity aligned (acceleration) and anti-aligned (deceleration) with the electric field. A time evolution of the energization for an ideal pickup ion is $q\vec{E} \cdot \vec{U}(O^+) = qE_z V_{E\times B} \sin(\Omega_c t)$, where q is the particle electric charge, E_z is the convection electric field, $V_{E\times B}$ is the E×B drift velocity, Ω_c is the angular gyrofrequency and t is time. In our case, the upstream conditions give $q\vec{E}\cdot \vec{U}(O^+) = 639$ eV/s $\sin(\Omega_c t)$ for a pickup ion, showing that the ideal energization varies from -639 eV/s to 639 eV/s, compatible with the values in Figure 4. Even though the energization rates of hundreds of eVs per second are high, planetary heavy ions are observed at tens of keV energies and such acceleration is available by the electric fields embedded in induced magnetospheres (*Futaana et al.*, 2017; *Jarvinen et al.*, 2018).

It is also important to notice that the ULF waves are not resonant with the gyromotion of the O^+ ions: In the upstream region, the O^+ gyroperiod is 104 s, which is well above the foreshock ULF wave period of 20–30 s. An O^+ ion reaches gyroperiods of $\leq$30 s only when the magnetic field strength is $\geq$34.7 nT, and such strong magnetic fields are limited to the low-altitude dayside magnetic barrier region under nominal upstream conditions at Venus. However, lighter species are more likely to become gyroresonant with the ULF waves (*Shimazu et al.*, 1996).

In order to isolate the effect of the ion foreshock on the O^+ energization, we performed a test run with a purely perpendicular upstream IMF relative to the solar wind flow. Under perpendicular IMF conditions, the bow shock is quasi-perpendicular throughout the simulation domain, and, consequently, no ion foreshock nor foreshock ULF waves form and there are no dawn-dusk asymmetries (*Jarvinen et al.*, 2013). In the test run, the O^+ escape rate does not show the significant fluctuations found in the Parker IMF case; the escape fluctuations had a peak-to-peak amplitudes less than 10% and periods less than 10 seconds. These weak fluctuations may be associated with turbulence or mirror mode waves in the magnetosheath (*Volwerk et al.*, 2016), or arise as a result of statistical macroparticle noise in the model. Conversely, the test run demonstrates that the statistical macroparticle noise is not the source of the fluctuations in the Parker spiral case.

As the wave modulation of the ion escape may occur also at Mars (*Kallio et al.*, 2006), we will focus future studies on the role of the magnetosheath wave activity and the dynamics of the induced magnetospheres on the heavy ion energization and escape at both Venus and Mars (*Futaana et al.*, 2017; *Dimmock et al.*, 2018; *Girazian et al.*, 2019). Furthermore, foreshock waves upstream of the quasi-parallel bow shock can couple with the low-altitude proton fluxes via the energetic neutral atom (ENA) production at Mars (*Fowler et al.*, 2019), but it is still an open question how the charge exchange, electron impact ionization and ionospheric photochemistry processes are affected by the ULF waves (*Yamauchi et al.*, 2015; *Mazelle et al.*, 2018), what are the ULF wave properties and their effect on the cold ion escape in or near the ionosphere and further in the tail (*Dubinin and Fraenz*, 2016; *Omidi et al.*, 2020), or how the ULF modulation of the escape and energization of heavy ions works under different upstream conditions, including flow-aligned IMF cases when the ion pickup is not a significant source of planetary ion acceleration (*Luhmann et al.*, 1993). Resolving the contribution of the ULF waves on the ion escape for different upstream conditions and ionization processes allows us to assess the evolutionary significance of its contribution on the atmospheric erosion at unmagnetized planets.

5 Conclusions

We analyze the Venus-solar wind interaction using a global hybrid simulation, which demonstrates a strong modulation of the O^+ ion energization and escape by the foreshock ULF waves. Consistent with the pickup of planetary ions by the solar wind convective electric field (rather than gyroresonance), the O^+ energization is modulated by the ULF waves in the upstream, magnetosheath and low-altitude regions leading to the 25% peak-to-peak fluctuations in the global escape rate from the simulation domain. This mechanism is sufficiently effective that it needs to be accounted for in the interpretation of heavy ion observations and possible acceleration of planetary ions by plasma waves at Venus and Mars.

Acknowledgments

The work was supported by the Academy of Finland (Decision No. 310444). The authors thank the ISSI (International Space Science Institute) and ISSI-BJ (International Space Science Institute Beijing) team "Dayside Transient Phenomena and Their Impact on the Magnetosphere-Ionosphere" for discussions and suggestions. Figure 1 was created using the VisIt open-source visualisation tool (*Childs et al.*, 2012). Global three-dimensional hybrid simulations were performed using the RHybrid simulation platform, which is available under an open-source license by the Finnish Meteorological Institute (`https://github.com/fmihpc/rhybrid/`). The simulation code version used in this study is archived under DOI: 10.5281/zenodo.3624041.

6 References

References

Brain, D., S. Barabash, A. Boesswetter, S. Bougher, S. Brecht, G. Chanteur, D. Hurley, E. Dubinin, X. Fang, M. Fraenz, J. Halekas, E. Harnett, M. Holmstrom, E. Kallio, H. Lammer, S. Ledvina, M. Liemohn, K. Liu, J. Luhmann, Y. Ma, R. Modolo, A. Nagy, U. Motschmann, H. Nilsson, H. Shinagawa, S. Si-

Table 1. Setup of the global Venus hybrid model and upstream undisturbed solar wind (SW) and interplanetary magnetic field (IMF) conditions after *Slavin and Holzer* (1981). The spiral angle is defined as $\arctan(B_y/B_x)$. *) Note on the calculation of the sonic and magnetosonic Mach numbers and plasma beta: we use the polytropic index of $\gamma = 5/3$ and have a mass-less electron fluid in the model.

Parameter	Symbol	Value
Box size [R_V]	$x \times y \times z$	$(-4...3) \times (-6...3) \times (-3...3)$
Number of grid cells	$n_x \times n_y \times n_z$	$280 \times 360 \times 240$
Grid cell size	Δx^3	$(151\ \mathrm{km})^3 = (R_\mathrm{V}/40)^3$
Number of macroions	$\mathcal{M}$	212 per cell on average
Timestep	Δt	10 ms
SW bulk velocity vector	$\vec{U}_\mathrm{SW}$	$[v_x = -430, v_y = 0, v_z = 0]$ km/s
SW H$^+$ temperature	$T_\mathrm{SW}(\mathrm{H}^+)$	1.0×10^5 K
SW He^{++} temperature	$T_\mathrm{SW}(\mathrm{He}^{++})$	$3.5 \times 10^5\ \mathrm{K} = 3.5 T_\mathrm{SW}(\mathrm{H}^+)$
SW H$^+$ density	$n(\mathrm{H}^+)$	14 cm^{-3}
SW He^{++} density	$n(\mathrm{He}^{++})$	$0.56\ \mathrm{cm}^{-3} = 0.04 n(\mathrm{H}^+)$
Electron temperature	T_e	10^4 K
IMF vector	$\vec{B}_\mathrm{SW}$	$[B_x = -8.09, B_y = 5.88, B_z = 0]$ nT
IMF magnitude	$\lvert\vec{B}_\mathrm{SW}\rvert$	10 nT
IMF spiral angle	ϕ	36° (away sector)
Convection electric field	$\vec{E}_\mathrm{SW}$	$[E_x = 0, E_y = 0, E_z = 2.5]$ mV/m
Alfvén Mach number	M_A	7.9
Sonic Mach number	M_S	11.7*
Magnetosonic Mach number	M_ms	6.6*
Plasma beta	β	0.55*
Zero B (superconducting shell) radius	R_η	$6351.8\ \mathrm{km} = R_\mathrm{V} + 300\ \mathrm{km}$
Obstacle resistivity	$\eta_\mathrm{a}(r < R_\eta)$	0
Plasma resistivity	$\eta_\mathrm{a}(r \geq R_\eta)$	$0.01 \times \mu_0 \Delta x^2/\Delta t$
Particle absorption radius	R_p	$6251.8\ \mathrm{km} = R_\mathrm{V} + 200\ \mathrm{km}$
H$^+$ photoion prod. rate		$6.42 \times 10^{24}\ \mathrm{s}^{-1}$
O$^+$ photoion prod. rate		$4.09 \times 10^{24}\ \mathrm{s}^{-1}$
O$^+$ ionospheric emis. rate		$1.0 \times 10^{25}\ \mathrm{s}^{-1}$
Ionospheric emis. radius		$R_\mathrm{V} + 400$ km
Solar EUV photo rates		solar minimum

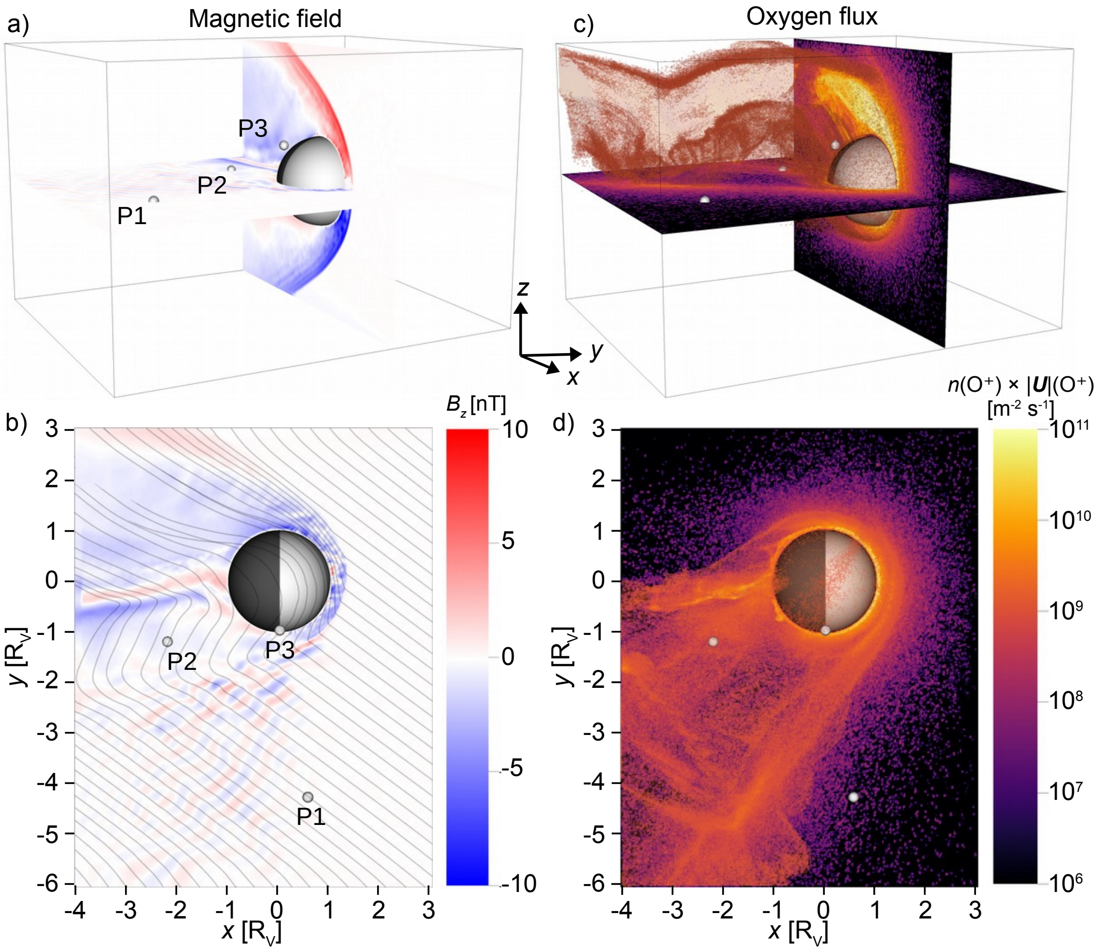

Figure 1. A snapshot of (a-b) the B_z component of the magnetic field and (c-d) the O$^+$ bulk flux at $t = 350$ s in the analyzed simulation run. The parameters are shown on the $z = 0$ and $y = 0$ planes. A partially transparent three-dimensional volume rendering of the O$^+$ bulk flux in regions with $n(\mathrm{O}^+) \times |\vec{U}|(\mathrm{O}^+) \geq 10^9$ m^{-2} s^{-1} is shown in panels (c) and (d). Magnetic field lines are shown projected on the $z = 0$ plane in panel (b). The three-dimensional field line tracing was started in the upstream region at $z = 2000$ km. Small grey spheres give the location of the points P1-P3. Big grey-black sphere has the radius of Venus for context. See Movie S01 in the supplementary material for temporal evolution of the parameters.

mon, and N. Terada (2010), A comparison of global models for the solar wind interaction with Mars, *Icarus*, *206*, 139–151, doi:10.1016/j.icarus.2009.06.030.

Brain, D. A., F. Bagenal, Y. J. Ma, H. Nilsson, and G. Stenberg Wieser (2016), Atmospheric escape from unmagnetized bodies, *J. Geophys. Res.*, *121*(12), 2364–2385, doi:10.1002/2016JE005162.

Childs, H., E. Brugger, B. Whitlock, J. Meredith, S. Ahern, D. Pugmire, K. Biagas, M. Miller, C. Harrison, G. H. Weber, H. Krishnan, T. Fogal, A. Sanderson, C. Garth, E. W. Bethel, D. Camp, O. Rübel, M. Durant, J. M. Favre, and P. Navrátil (2012), VisIt: An End-User Tool For Visualizing and Analyzing Very Large Data, in *High Performance Visualization–Enabling Extreme-Scale Scientific Insight*, pp. 357–372, CRC Press, New York.

Collinson, G., L. B. Wilson, N. Omidi, D. Sibeck, J. Espley, C. M. Fowler, D. Mitchell, J. Grebowsky, C. Mazelle, S. Ruhunusiri, J. Halekas, R. Frahm, T. Zhang, Y. Futaana, and B. Jakosky (2018), Solar Wind Induced Waves in the Skies of Mars: Ionospheric Compression, Energization, and Escape Resulting From the Impact of Ultralow Frequency Magnetosonic Waves Generated Upstream of the Martian Bow Shock, *J. Geophys. Res.*, *123*(9), 7241–7256, doi:10.1029/2018JA025414.

Dimmock, A. P., M. Alho, E. Kallio, S. A. Pope, T. L. Zhang, E. Kilpua, T. I. Pulkkinen, Y. Futaana, and A. J. Coates (2018), The Response of the Venusian Plasma Environment to the Passage of an ICME: Hybrid Simulation Results and Venus Express Observations, *J. Geophys. Res.*, *123*(5), 3580–3601, doi:10.1029/2017JA024852.

Dong, Y., X. Fang, D. A. Brain, J. P. McFadden, J. S. Halekas, J. E. P. Connerney, F. Eparvier, L. Andersson, D. Mitchell, and B. M. Jakosky (2017), Seasonal variability of Martian ion escape through the plume and tail from MAVEN observations, *J. Geophys. Res.*, *122*(4), 4009–4022, doi:10.1002/2016JA023517.

Dubinin, E., and M. Fraenz (2016), Ultra-Low-Frequency Waves at Venus and Mars, *Washington DC American Geophysical Union Geophysical Monograph Series*, *216*, 343–364, doi:10.1002/9781119055006.ch20.

Dubinin, E., M. Fraenz, A. Fedorov, R. Lundin, N. Edberg, F. Duru, and O. Vaisberg (2011), Ion Energization and Escape on Mars and Venus, *Space Sci. Rev.*, *162*, 173–211, doi:10.1007/s11214-011-9831-7.

Eastwood, J. P., E. A. Lucek, C. Mazelle, K. Meziane, Y. Narita, J. Pickett, and R. A. Treumann (2005), The Foreshock, *Space Sci. Rev.*, *118*, 41–94, doi:10.1007/s11214-005-3824-3.

Fedorov, A., S. Barabash, J.-A. Sauvaud, Y. Futaana, T. L. Zhang, R. Lundin, and C. Ferrier (2011), Measurements of the ion escape rates from Venus for solar minimum, *J. Geophys. Res.*, *116*, A07220, doi:10.1029/2011JA016427.

Fowler, C. M., J. Halekas, S. Schwartz, K. A. Goodrich, J. R. Gruesbeck, and M. Benna (2019), The Modulation of Solar Wind Hydrogen Deposition in the Martian Atmosphere by Foreshock Phenomena, *J. Geophys. Res.*, *124*(8), 7086–7097, doi:10.1029/2019JA026938.

Franco, A. M. S., M. Fränz, E. Echer, M. J. A. Bolzan, and T. L. Zhang (2020), The correlation length of ULF waves around Venus: VEX observations, *Planet. Space Sci.*, *180*, 104761, doi:10.1016/j.pss.2019.104761.

Fränz, M., E. Echer, A. Marques de Souza, E. Dubinin, and T. L. Zhang (2017), Ultra low frequency waves at Venus: Observations by the Venus Express spacecraft, *Planet. Space Sci.*, *146*, 55–65, doi:10.1016/j.pss.2017.08.011.

Futaana, Y., G. Stenberg Wieser, S. Barabash, and J. G. Luhmann (2017), Solar Wind Interaction and Impact on the Venus Atmosphere, *Space Sci. Rev.*, *212*(3-4), 1453–1509, doi:10.1007/s11214-017-0362-8.

Girazian, Z., J. Halekas, D. D. Morgan, A. J. Kopf, D. A. Gurnett, and F. Chu (2019), The Effects of Solar Wind Dynamic Pressure on the Structure of the Topside Ionosphere of Mars, *Geophys. Res. Lett.*, *46*(15), 8652–8662, doi:10.1029/2019GL083643.

Greenwood, J. P., S.-i. Karato, K. E. Vand er Kaaden, K. Pahlevan, and T. Usui (2018), Water and Volatile Inventories of Mercury, Venus, the Moon, and Mars, *Space Sci. Rev.*, *214*(5), 92, doi:10.1007/s11214-018-0526-1.

Jarvinen, R., and E. Kallio (2014), Energization of planetary pickup ions in the solar system, *J. Geophys. Res.*, *119*, 219–236, doi:10.1002/2013JE004534.

Jarvinen, R., E. Kallio, P. Janhunen, S. Barabash, T. L. Zhang, V. Pohjola, and I. Sillanpää (2009), Oxygen ion escape from Venus in a global hybrid simulation: role of the ionospheric O^+ ions, *Ann. Geophys.*, *27*, 4333–4348.

Jarvinen, R., E. Kallio, and S. Dyadechkin (2013), Hemispheric asymmetries of the Venus plasma environment, *J. Geophys. Res.*, *118*, 4551–4563, doi: 10.1002/jgra.50387.

Jarvinen, R., D. A. Brain, and J. G. Luhmann (2016), Dynamics of planetary ions in the induced magnetospheres of Venus and Mars, *Planet. Space Sci.*, *127*, 1–14, doi:10.1016/j.pss.2015.08.012.

Jarvinen, R., D. A. Brain, R. Modolo, A. Fedorov, and M. Holmström (2018), Oxygen Ion Energization at Mars: Comparison of MAVEN and Mars Express Observations to Global Hybrid Simulation, *J. Geophys. Res.*, *123*, 1678–1689, doi:10.1002/2017JA024884.

Jarvinen, R., M. Alho, E. Kallio, and T. I. Pulkkinen (2020), Ultra-low-frequency waves in the ion foreshock of Mercury: a global hybrid modelling study, *Mon. Notices Royal Astron. Soc.*, *491*(3), 4147–4161, doi:10.1093/mnras/stz3257.

Kallio, E., and P. Janhunen (2003), Modelling the solar wind interaction with Mercury by a quasi-neutral hybrid model, *Ann. Geophys.*, *21*, 2133–2145.

Kallio, E., A. Fedorov, S. Barabash, P. Janhunen, H. Koskinen, W. Schmidt, R. Lundin, H. Gunell, M. Holmström, Y. Futaana, M. Yamauchi, A. Grigoriev, J. D. Winningham, R. Frahm, and J. R. Sharber (2006), Energisation of O^+ and O_2^+ Ions at Mars: An Analysis of a 3-D Quasi-Neutral Hybrid Model Simulation, *Space Sci. Rev.*, *126*, 39–62, doi:10.1007/s11214-006-9120-z.

Kallio, E., K. Liu, R. Jarvinen, V. Pohjola, and P. Janhunen (2010), Oxygen ion escape at Mars in a hybrid model: High energy and low energy ions, *Icarus*, *206*, 152–163, doi:10.1016/j.icarus.2009.05.015.

Keiling, A., D.-H. Lee, and V. Nakariakov (2016), Low-Frequency Waves in Space Plasmas, *Washington DC American Geophysical Union Geophysical Monograph Series*, *216*.

Ledvina, S. A., Y. Ma, and E. Kallio (2008), Modeling and Simulating Flowing Plasmas and Related Phenomena, *Space Sci. Rev.*, *139*, 143–189, doi: 10.1007/s11214-008-9384-6.

Liemohn, M. W., B. C. Johnson, M. Fränz, and S. Barabash (2014), Mars Express observations of high altitude planetary ion beams and their relation to the "energetic plume" loss channel, *J. Geophys. Res.*, *119*(12), 9702–9713, doi: 10.1002/2014JA019994.

Luhmann, J. G., M. Tatrallyay, C. T. Russell, and D. Winterhalter (1983), Magnetic field fluctuations in the Venus magnetosheath, *Geophys. Res. Lett.*, *10*(8), 655–658, doi:10.1029/GL010i008p00655.

Luhmann, J. G., C. T. Russell, J. L. Phillips, and A. Barnes (1987), On the role of the quasi-parallel bow shock in ion pickup - A lesson from Venus?, *J. Geophys. Res.*, *92*, 2544–2550, doi:10.1029/JA092iA03p02544.

Luhmann, J. G., T. Zhang, S. M. Petrinec, C. T. Russell, P. Gazis, and A. Barnes (1993), Solar cycle 21 effects on the Interplanetary Magnetic Field and related parameters at 0.7 and 1.0 AU, *J. Geophys. Res.*, *98*, 5559–5572, doi: 10.1029/92JA02235.

Lundin, R. (2011), Ion Acceleration and Outflow from Mars and Venus: An Overview, *Space Sci. Rev.*, *162*, 309–334, doi:10.1007/s11214-011-9811-y.

Lundin, R., S. Barabash, E. Dubinin, D. Winningham, and M. Yamauchi (2011), Low-altitude acceleration of ionospheric ions at Mars, *Geophys. Res. Lett.*, *38*(8), L08108, doi:10.1029/2011GL047064.

Mazelle, C. X., K. Meziane, D. L. Mitchell, P. Garnier, J. R. Espley, A. M. Hamza, J. Halekas, and B. M. Jakosky (2018), Evidence for Neutrals-Foreshock Electrons Impact at Mars, *Geophys. Res. Lett.*, *45*(9), 3768–3774, doi:10.1002/2018GL077298.

McComas, D. J., H. E. Spence, C. T. Russell, and M. A. Saunders (1986), The average magnetic field draping and consistent plasma properties of the Venus magnetotail, *J. Geophys. Res.*, *91*, 7939–7953, doi:10.1029/JA091iA07p07939.

Nilsson, H., I. A. Barghouthi, R. Slapak, A. I. Eriksson, and M. André (2012), Hot and cold ion outflow: Spatial distribution of ion heating, *J. Geophys. Res.*, *117*(A11), A11201, doi:10.1029/2012JA017974.

Nordström, T., G. Stenberg, H. Nilsson, S. Barabash, and T. L. Zhang (2013), Venus ion outflow estimates at solar minimum: Influence of reference frames and disturbed solar wind conditions, *J. Geophys. Res.*, *118*, 3592–3601, doi:10.1002/jgra.50305.

Omidi, N., G. Collinson, and D. Sibeck (2017), Structure and Properties of the Foreshock at Venus, *J. Geophys. Res.*, *122*(10), 10,275–10,286, doi:10.1002/2017JA024180.

Omidi, N., G. Collinson, and D. Sibeck (2020), Foreshock Bubbles at Venus: Hybrid Simulations and VEX Observations, *J. Geophys. Res.*, *125*(2), e27056, doi:10.1029/2019JA027056.

Persson, M., Y. Futaana, A. Fedorov, H. Nilsson, M. Hamrin, and S. Barabash (2018), H^+/O^+ Escape Rate Ratio in the Venus Magnetotail and its Dependence on the Solar Cycle, *Geophys. Res. Lett.*, *45*(20), 10,805–10,811, doi:10.1029/2018GL079454.

Russell, C. T., E. Chou, J. G. Luhmann, P. Gazis, L. H. Brace, and W. R. Hoegy (1988), Solar and interplanetary control of the location of the Venus bow shock, *J. Geophys. Res.*, *93*, 5461–5469, doi:10.1029/JA093iA06p05461.

Shan, L., Q. Lu, M. Wu, X. Gao, C. Huang, T. Zhang, and S. Wang (2014), Transmission of large-amplitude ULF waves through a quasi-parallel shock at Venus, *J. Geophys. Res.*, *119*(1), 237–245, doi:10.1002/2013JA019396.

Shan, L., C. Mazelle, K. Meziane, M. Delva, Q. Lu, Y. S. Ge, A. Du, and T. Zhang (2016), Characteristics of quasi-monochromatic ULF waves in the Venusian foreshock, *J. Geophys. Res.*, *121*, 7385–7397, doi:10.1002/2016JA022876.

Shimazu, H., M. Tanaka, and S. Machida (1996), Behavior of heavy ions in a collisionless parallel shock generated by the solar wind and planetary plasma interactions, *J. Geophys. Res.*, *101*(A12), 27,565–27,572, doi:10.1029/96JA02343.

Slavin, J. A., and R. E. Holzer (1981), Solar wind flow about the terrestrial planets. I - Modeling bow shock position and shape, *J. Geophys. Res.*, *86*, 11,401–11,418, doi:10.1029/JA086iA13p11401.

Volwerk, M., D. Schmid, B. T. Tsurutani, M. Delva, F. Plaschke, Y. Narita, T. Zhang, and K.-H. Glassmeier (2016), Mirror mode waves in Venus's magnetosheath: solar minimum vs. solar maximum, *Ann. Geophys.*, *34*(11), 1099–1108, doi:10.5194/angeo-34-1099-2016.

Wei, Y., M. Fraenz, E. Dubinin, W. Wan, T. Zhang, Z. Rong, L. Chai, J. Zhong, R. Zhu, Y. Futaana, and S. Barabash (2017), Ablation of venusian oxygen ions by unshocked solar wind, *Science Bulletin*, *62*(24), 1669 – 1672, doi: https://doi.org/10.1016/j.scib.2017.11.006.

Yamauchi, M., R. Lundin, R. A. Frahm, J. A. Sauvaud, M. Holmström, and S. Barabash (2015), Oxygen foreshock of Mars, *Planet. Space Sci.*, *119*, 48–53, doi:10.1016/j.pss.2015.08.003.

Yau, A. W., E. G. Shelley, W. K. Peterson, and L. Lenchyshyn (1985), Energetic auroral and polar ion outflow at DE 1 altitudes: Magnitude, composition, magnetic activity dependence, and long-term variations, *J. Geophys. Res.*, *90*(A9), 8417–8432, doi:10.1029/JA090iA09p08417.

Zhang, T. L., M. Delva, W. Baumjohann, M. Volwerk, C. T. Russell, S. Barabash, M. Balikhin, S. Pope, K. H. Glassmeier, K. Kudela, C. Wang, Z. Vörös, and W. Zambelli (2008a), Initial Venus Express magnetic field observations of the Venus bow shock location at solar minimum, *Planet. Space Sci.*, *56*(6), 785–789, doi:10.1016/j.pss.2007.09.012.

Zhang, T. L., M. Delva, W. Baumjohann, M. Volwerk, C. T. Russell, H. Y. Wei, C. Wang, M. Balikhin, S. Barabash, H. U. Auster, and K. Kudela (2008b), Induced magnetosphere and its outer boundary at Venus, *J. Geophys. Res.*, *113*(5), E00B20, doi:10.1029/2008JE003215.

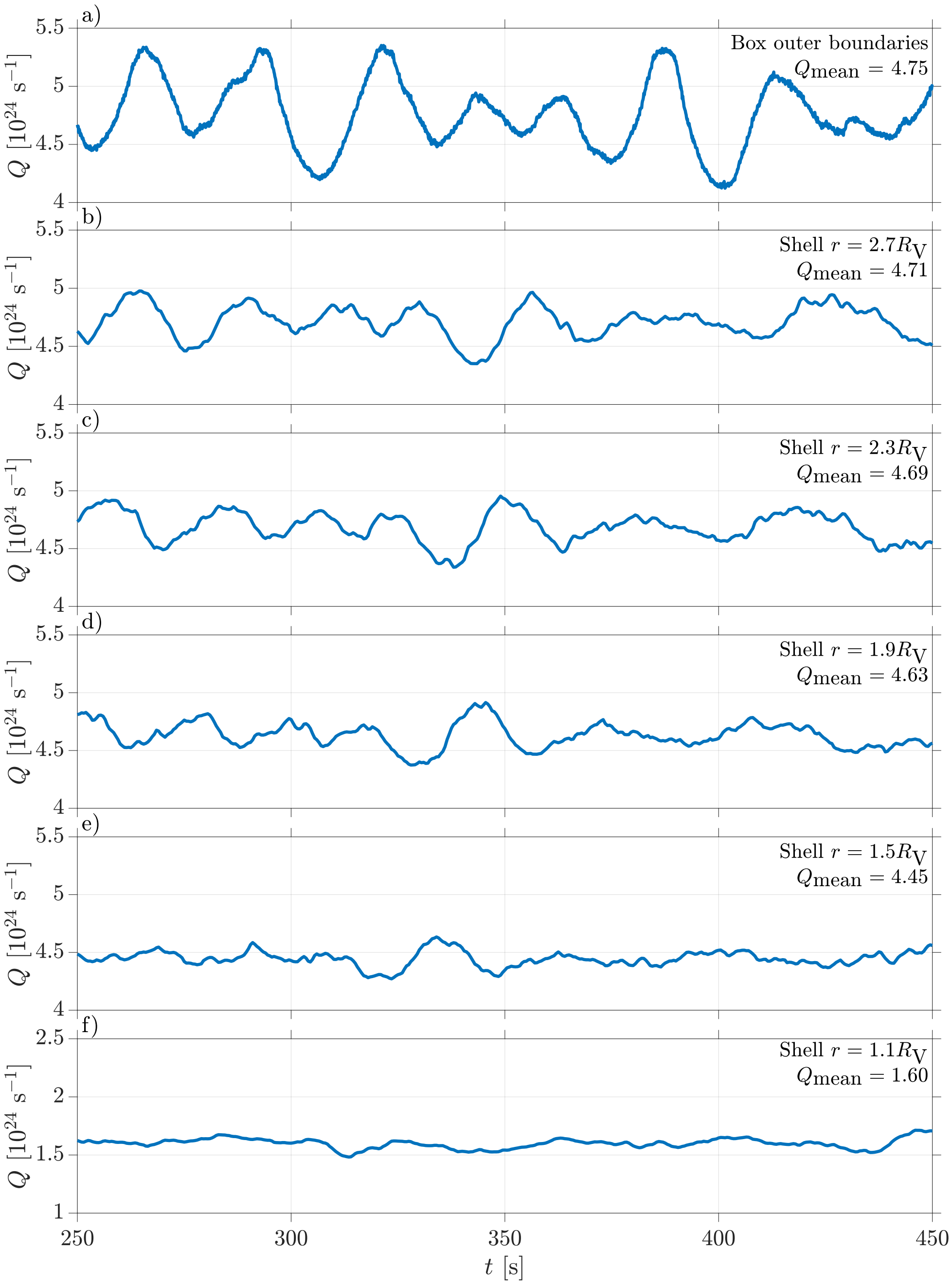

Figure 2. Time series of the O^+ (a) escape rate through the outer boundaries of the simulation domain and (b-f) net escape rate (outward-inward) at spherical shells at $r = 1.1 \dots 2.7\ R_V$. The escape rate in panel (a) was determined as a sum of particles hitting the outer boundaries and being removed from the run. The escape rate in panels (b-f) was calculated by integrating the radial particle bulk flux over each shell ($Q = \sum n(O^+) \times U_r(O^+)$, where n is the number density and U_r is the radial component of the bulk velocity).

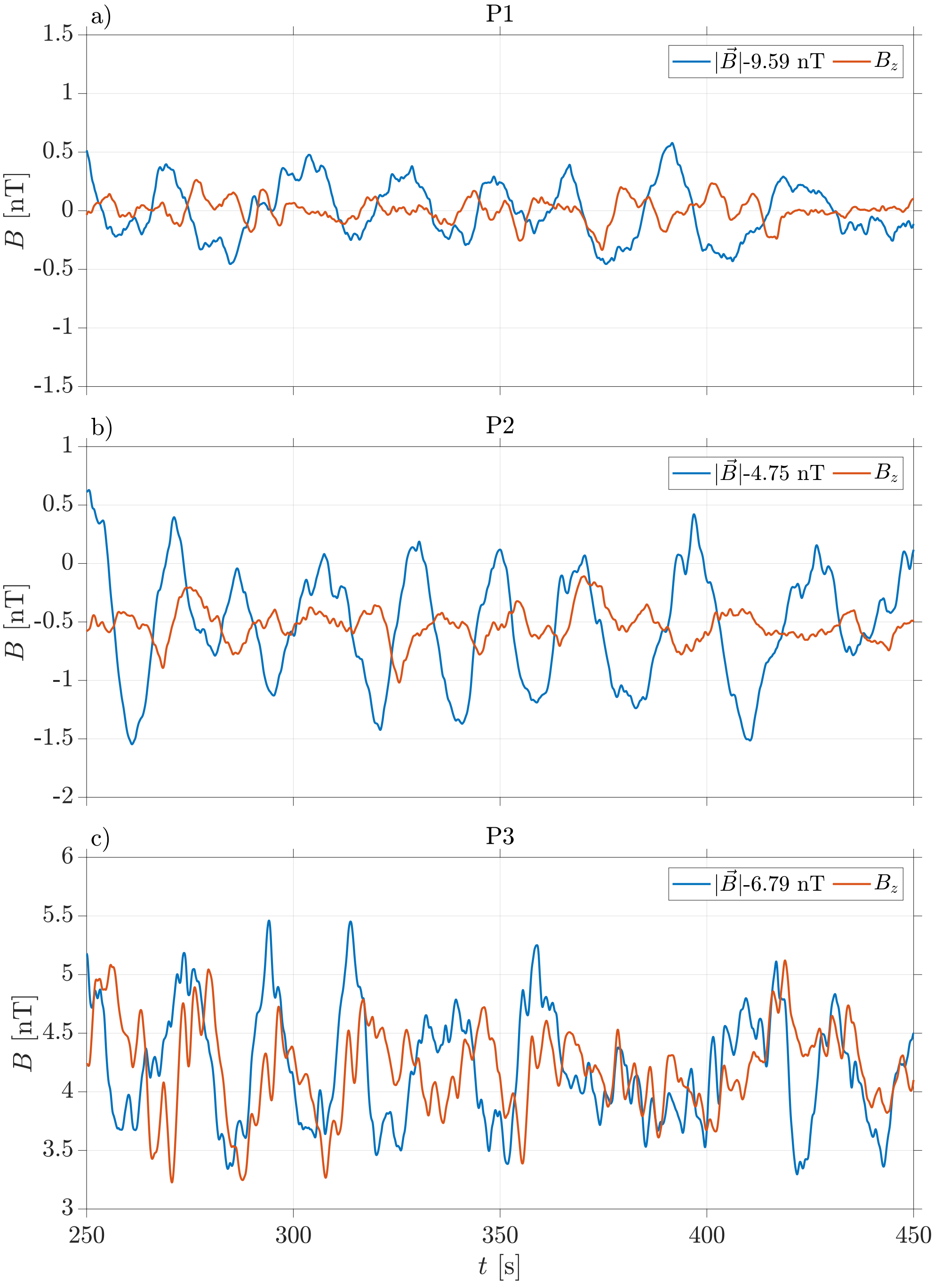

268 **Figure 3.** Time series of the magnetic field magnitude (blue curve) and B_z (red curve) at the
269 points P1-P3, which are shown in Figure 1. The magnitude was translated to the same mean
270 value as the z-component.

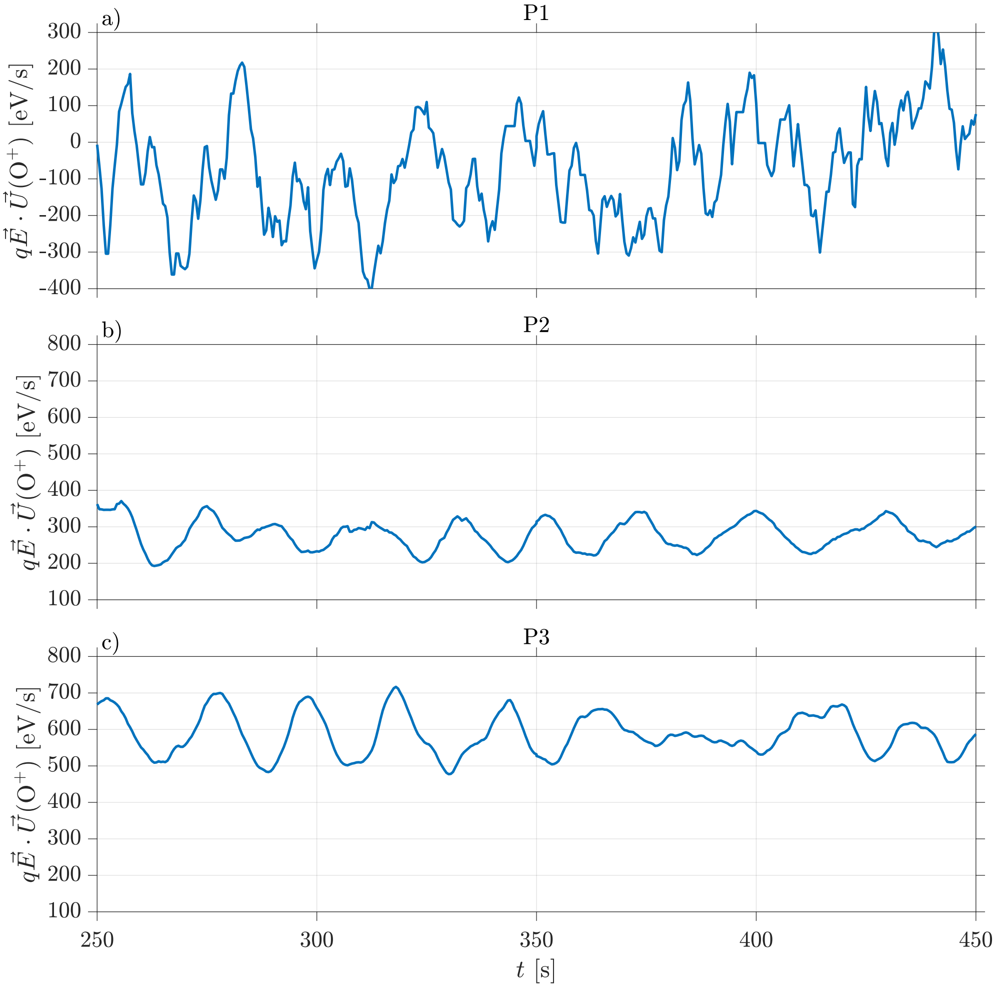

Figure 4. Time series of the O^+ energization rate $q\vec{E} \cdot \vec{U}(\mathrm{O}^+)$ at the points P1-P3, which are shown in Figure 1. q is the particle electric charge, $\vec{E}$ is the electric field and $\vec{U}(\mathrm{O}^+)$ is the O^+ bulk velocity. See Movies S02 and S03 in the supplementary material for temporal and spatial evolution of the energization.

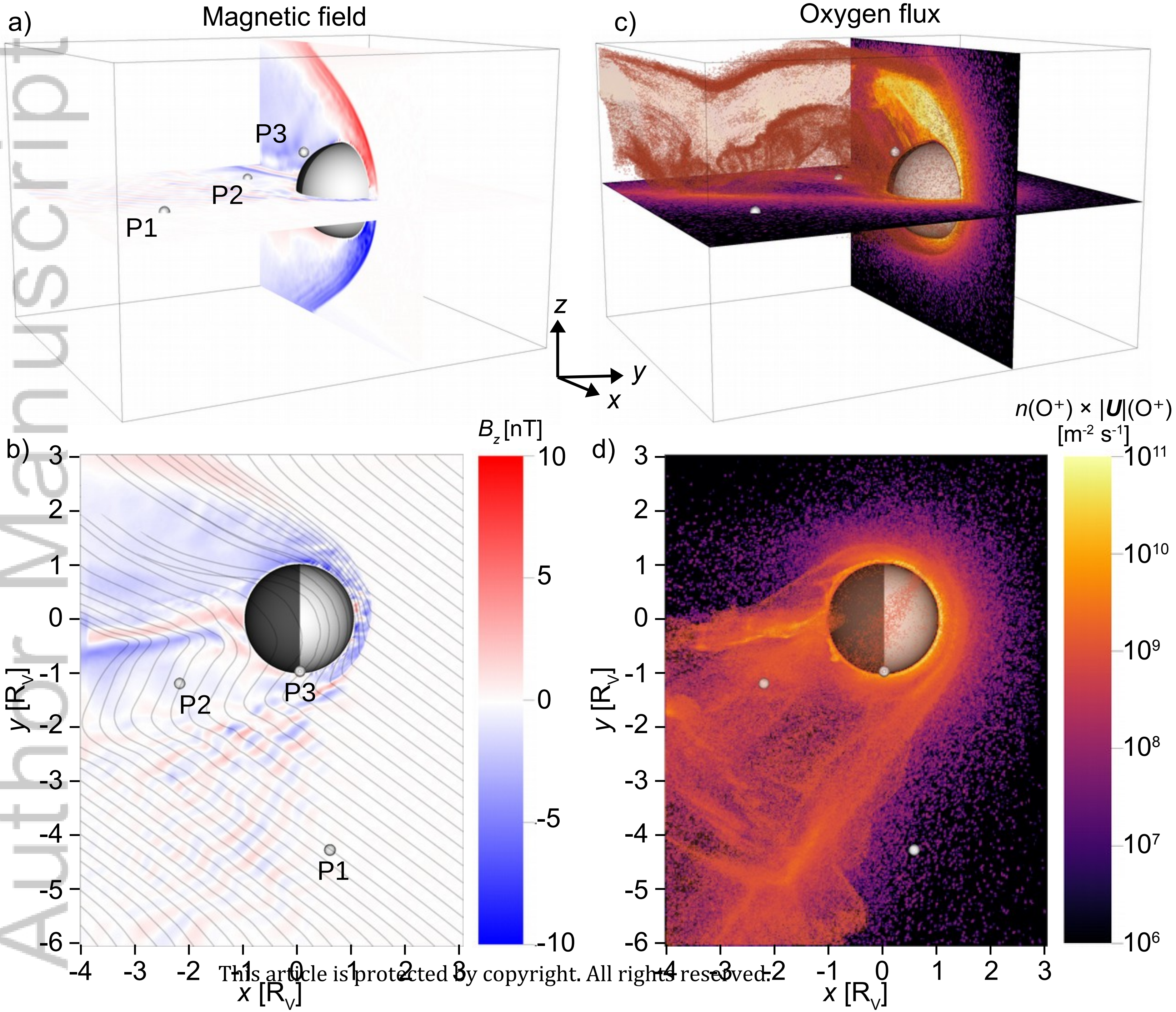
a)
Magnetic field
P3
P2
P1
c)
Oxygen flux
z
y
x
$n(O^+) \times |\boldsymbol{U}|(O^+)$
[m^{-2} s^{-1}]
b)
B_z [nT]
10
5
0
-5
-10
P2
P3
P1
y [R$_V$]
x [R$_V$]
3
2
1
0
-1
-2
-3
-4
-5
-6
-4
-3
-2
-1
0
1
2
3
d)
10^{11}
10^{10}
10^9
10^8
10^7
10^6
y [R$_V$]
x [R$_V$]

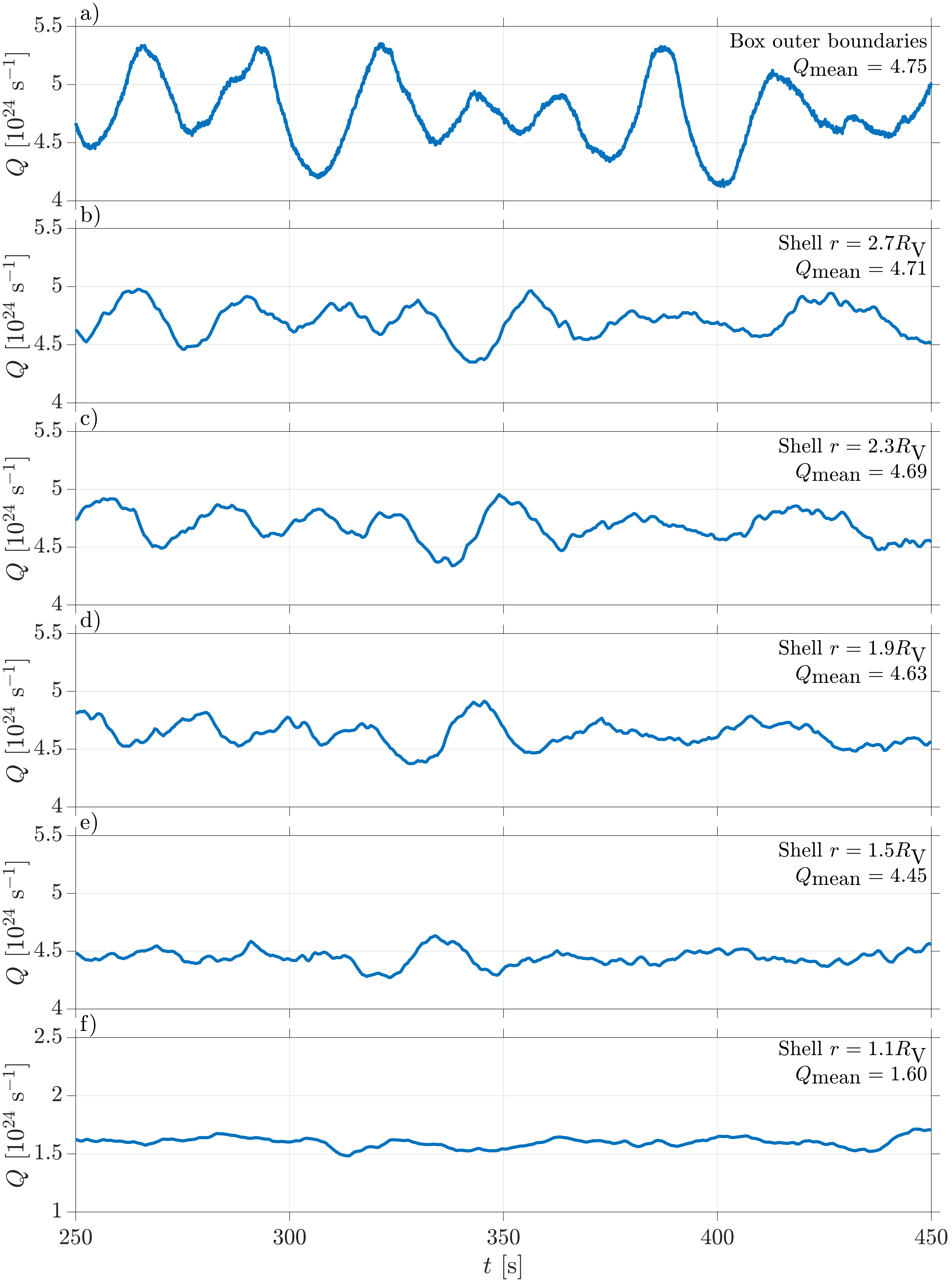
a)
b)
c)
d)
e)
f)
Box outer boundaries
Qmean = 4.75
Shell $r = 2.7R_V$
Qmean = 4.71
Shell $r = 2.3R_V$
Qmean = 4.69
Shell $r = 1.9R_V$
Qmean = 4.63
Shell $r = 1.5R_V$
Qmean = 4.45
Shell $r = 1.1R_V$
Qmean = 1.60
Q [10^{24} s^{-1}]
5.5
5
4.5
4
2.5
2
1.5
1
250
300
350
400
450
t [s]

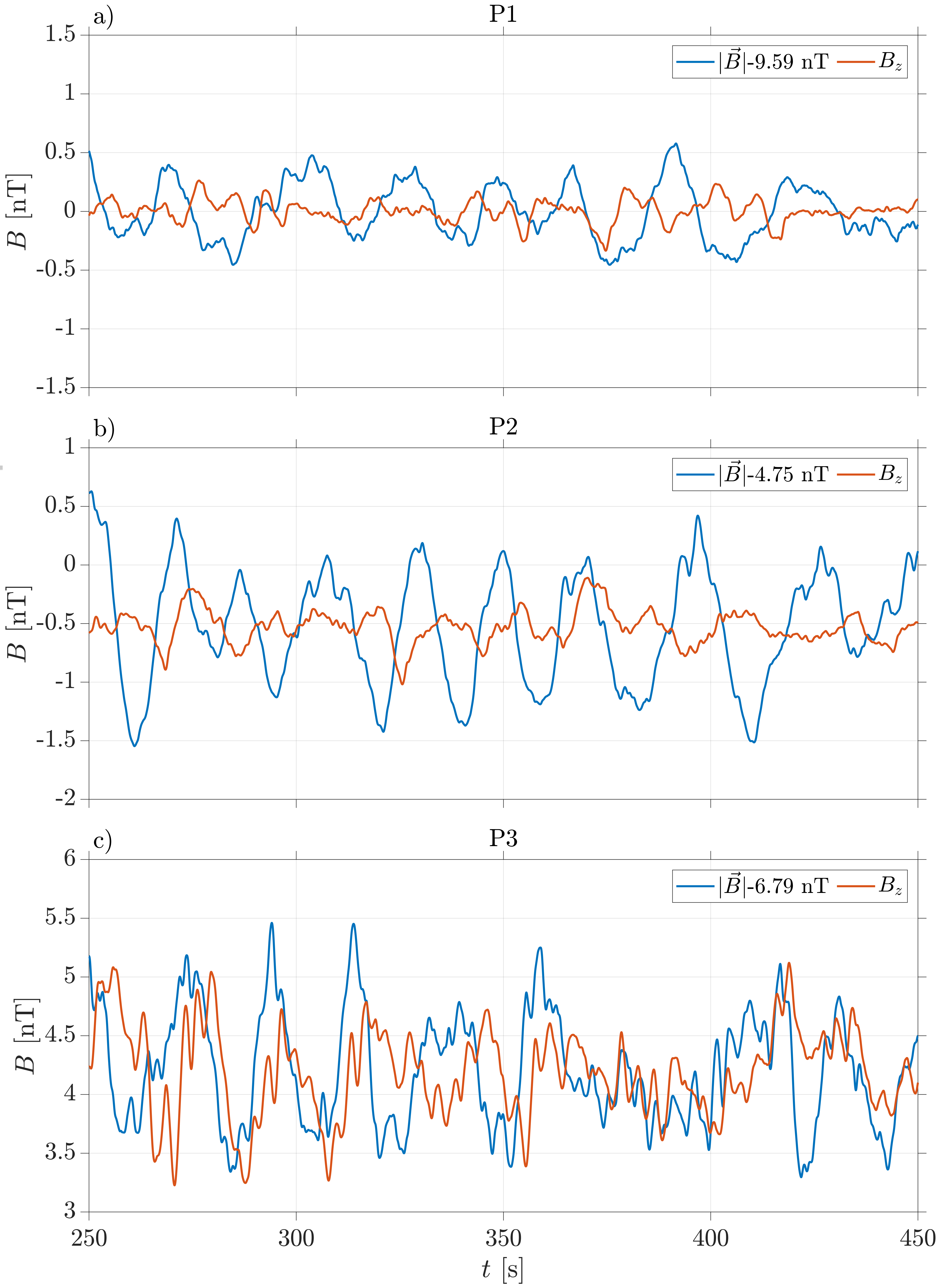
a)
P1
$|\vec{B}|$-9.59 nT
B_z
1.5
1
0.5
0
-0.5
-1
-1.5
B [nT]
b)
P2
$|\vec{B}|$-4.75 nT
B_z
1
0.5
0
-0.5
-1
-1.5
-2
B [nT]
c)
P3
$|\vec{B}|$-6.79 nT
B_z
6
5.5
5
4.5
4
3.5
3
B [nT]
250
300
350
400
450
t [s]

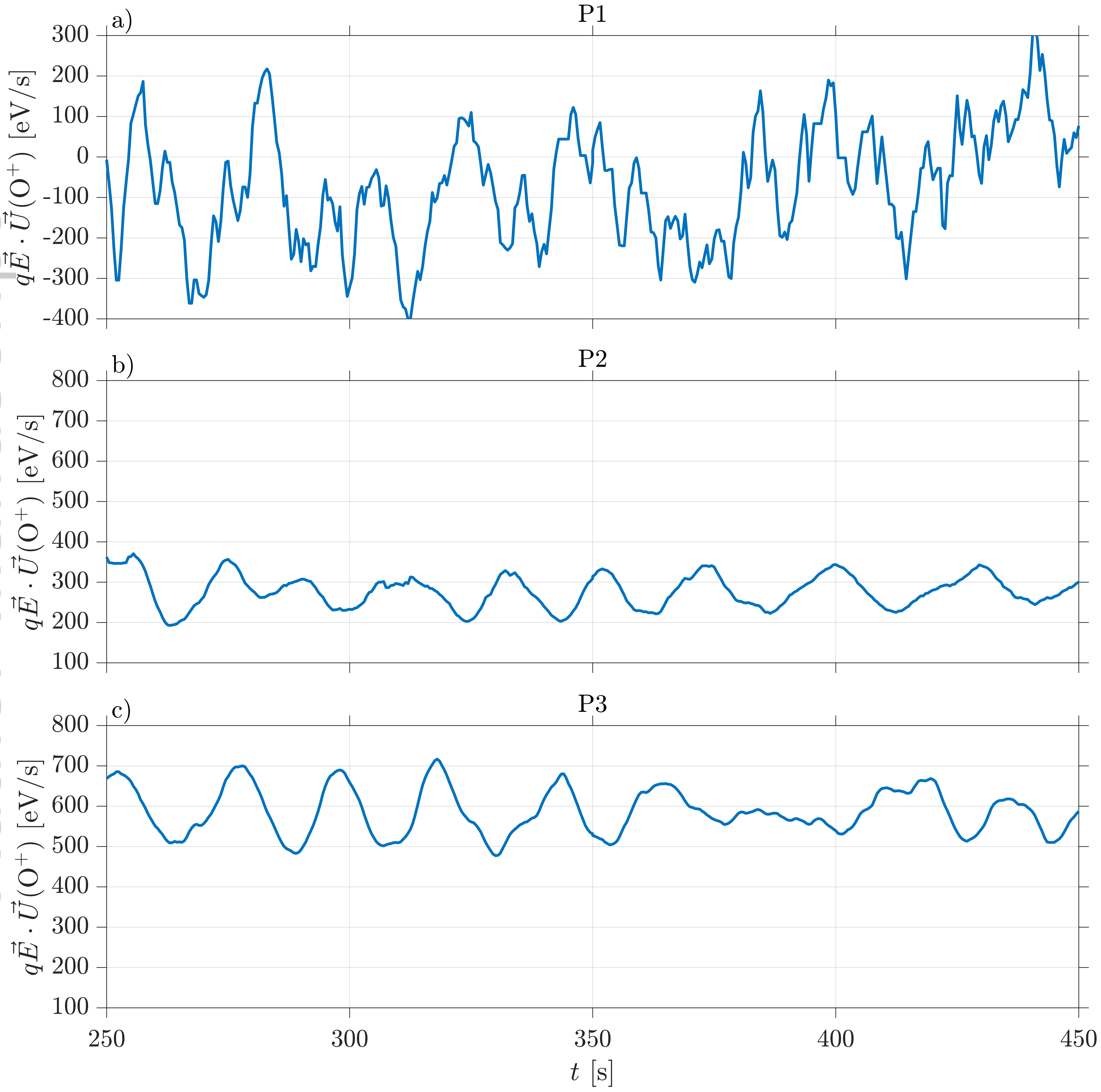
a)
P1
300
200
100
0
-100
-200
-300
-400
$q\vec{E}\cdot\vec{U}(\mathrm{O}^+)$ [eV/s]
b)
P2
800
700
600
500
400
300
200
100
$q\vec{E}\cdot\vec{U}(\mathrm{O}^+)$ [eV/s]
c)
P3
800
700
600
500
400
300
200
100
$q\vec{E}\cdot\vec{U}(\mathrm{O}^+)$ [eV/s]
250
300
350
400
450
t [s]